## STRUCTURAL BIOLOGY

MMOD-induced structural changes of hydroxylase in soluble methane monooxygenase

Hanseong Kim[1], Sojin An[1], Yeo Reum Park[2], Hara Jang[2], Heeseon Yoo[2], Sang Ho Park[1], Seung Jae Lee[2]*, Uhn-Soo Cho[1]*

Soluble methane monooxygenase in methanotrophs converts methane to methanol under ambient conditions. The maximum catalytic activity of hydroxylase (MMOH) is achieved through the interplay of its regulatory protein (MMOB) and reductase. An additional auxiliary protein, MMOD, functions as an inhibitor of MMOH; however, its inhibitory mechanism remains unknown. Here, we report the crystal structure of the MMOH-MMOD complex from *Methylosinus sporium* strain 5 (2.6 Å). Its structure illustrates that MMOD associates with the canyon region of MMOH where MMOB binds. Although MMOD and MMOB recognize the same binding site, each binding component triggers different conformational changes toward MMOH, which then respectively lead to the inhibition and activation of MMOH. Particularly, MMOD binding perturbs the di-iron geometry by inducing two major MMOH conformational changes, i.e., MMOH β subunit disorganization and subsequent His[147] dissociation with Fe1 coordination. Furthermore, 1,6-hexanediol, a mimic of the products of sMMO, reveals the substrate access route.

INTRODUCTION

Methanotrophs have an ability to use methane as their sole energy and carbon source (*1–3*). The critical enzymes participating in this conversion process are particulate methane monooxygenase (pMMO) and soluble methane monooxygenase (sMMO) (*4, 5*). In particular, the sMMO enzyme, which belongs to the bacterial multicomponent monooxygenase superfamily, catalyzes the following reaction (*1, 6–8*)

$$CH_4 + O_2 + 2H^+ + 2e^- \rightarrow CH_3OH + H_2O$$
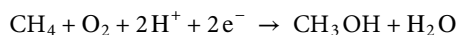
The sMMO operon houses six genes: *mmoX* (MMOHα), *mmoY* (MMOHβ), *mmoZ* (MMOHγ), *mmoC* (MMOR; MMO reductase), *mmoB* (MMOB; MMO regulatory protein), and *orfY* (MMOD; MMO inhibitory protein) (Fig. 1A) (*9–11*). Three genes (*mmoX*, *mmoY*, and *mmoZ*) encode the sequences for three subunits (MMOHα, MMOHβ, and MMOHγ) of sMMO hydroxylase, and the rest of the genes annotate three auxiliary components that modulate the catalytic activity of MMOH. The effectiveness of catalysis by sMMO is known to be linked to the interplay of three sMMO components: MMOH, MMOR, and MMOB. MMOH, which performs the chemical conversion of methane to methanol, is a homodimer of three subunits (α, β, and γ), with a glutamate- and histidine-coordinated nonheme di-iron center at each α subunit (*8, 12*). MMOR contains both a flavin adenine dinucleotide and a [2Fe-2S] ferredoxin domain that shuttle electrons from nicotinamide adenine dinucleotide (NADH) to the di-iron center in MMOH (*13*). MMOB is a regulatory component that alters reduction potentials at the di-iron center and helps the substrate gain access to the active site (*14, 15*).

The third auxiliary protein, MMOD, shows the inhibitory function by suppressing the catalytic activity of MMOH (*11, 16*). Recently, MMOD was also proposed as a "copper-switch," which may switch the protein expression of sMMO and pMMO depending on cellular copper concentration (*17, 18*). However, the exact physiological role and underlying molecular mechanism of MMOD has not been clearly demonstrated.

The crystal structure of MMOH and the nuclear magnetic resonance (NMR) structures of MMOB and two MMOR domains have been determined, and their potential roles in the catalytic reaction have been proposed (*19–24*). Nevertheless, the challenges in obtaining structures of MMOH complexed with its auxiliary proteins have made it difficult to fully elucidate the molecular mechanism by which MMOH catalyzes its substrates through the dynamic association with its auxiliary components. We previously reported the crystal structure of the MMOH-MMOB complex at 2.9-Å resolution (*14*). Structural studies of the MMOH-MMOB complex have addressed key questions about how MMOB changes the reduction potential of MMOH by inducing a geometric change of the di-iron center and opens the substrate access cavity. However, a deeper understanding of the enzymatic mechanisms of methane hydroxylation catalyzed by MMOH requires additional structural information. In particular, the role of other auxiliary proteins such as MMOR and MMOD in modulating the catalytic activity of MMOH upon binding, as well as the ingress and egress pathways of substrates and products in sMMO, has been only speculated and not structurally validated as yet.

Here, we report the crystal structure of the MMOH-MMOD complex from *Methylosinus sporium* strain 5 at 2.6-Å resolution. Although structurally distinct, MMOD and MMOB share the same binding site of MMOH, also known as the canyon region, for their association. MMOD binding, however, induces different sequences of conformational changes in MMOH compared to MMOB by (i) disorganizing the N-terminal region of MMOHβ, (ii) inducing the translational movement of helices B and C within MMOHα, and (iii) subsequently disrupting the di-iron geometry by dissociation with His[147] from Fe1 coordination. Therefore, MMOD performs its unique dual inhibitory function by competing with MMOB and, at the same time, by suppressing the formation of catalytic intermediates. In addition, we could structurally validate a long-standing hypothesis that MMOHα cavities support the passage of the substrate and product to and from the active site by visualizing 1,6-hexanediol—a product analog—at connected MMOHα cavities.

[1]Department of Biological Chemistry, University of Michigan, Ann Arbor, MI 48109, USA. [2]Department of Chemistry, Chonbuk National University, Jeonju 54896, Republic of Korea.
*Corresponding author. Email: slee026@jbnu.ac.kr (S.J.L.); uhnsoo@med.umich.edu (U.-S.C.)
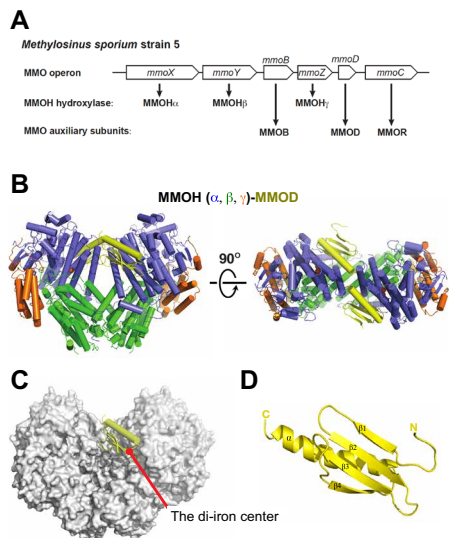
Fig. 1. Crystal structure of the MMOH-MMOD complex. (A) Schematic overview of the sMMO operon in *M. sporium* strain 5. (B) Front and top views of the MMOH-MMOD complex. MMOH is shown using a cartoon model (α subunit, blue; β subunit, green; and γ subunit, orange); MMOD is colored yellow, and the orange balls represent di-irons. (C) Front view of the MMOH-MMOD complex. MMOH is shown using a surface representation model (white), and MMOD (yellow) is shown in cartoon form. Red dot marks the location of the di-iron center in MMOH. (D) MMOD contains a ββββα-fold, which is shown in cartoon form. Illustrations of the protein structure used in all figures were generated with PyMOL (DeLano Scientific LLC).

RESULTS

MMOD associates with MMOH through the canyon region of MMOHα

To elucidate the molecular mechanism by which MMOD regulates the catalytic activity of MMOH, we determined the crystal structure of the MMOH-MMOD complex from *M. sporium* strain 5 at 2.6-Å resolution (Fig. 1B). The initial electron density map of the MMOH-MMOD complex was calculated by molecular replacement using *Methylosinus trichosporium* OB3b MMOH as the search model [Protein Data Bank (PDB) ID: 1MHY] (20). *M. trichosporium* OB3b MMOH and *M. sporium* strain 5 MMOH enzymes are highly homologous, sharing primary sequence identity of 97, 88, and 87% of the α, β, and γ subunits, respectively (fig. S1, A and B). The crystal structure of the MMOH-MMOD complex revealed that two copies of MMOD interacted symmetrically with MMOH via its canyon region (Fig. 1, B and C). The conserved core region of MMOD (residues 8 to 71) had a well-ordered structure and harbored a ββββα-fold architecture with four N-terminal antiparallel β strands and a long C-terminal α helix (Fig. 1D and fig. S1C). Residues 1 to 11 and 76 to 111 of MMOD, which are less conserved among other strains and predicted to be unstructured, were disordered in the crystal structure.

Furthermore, it was found that MMOD was bound to helices E, F, and H of the MMOHα (MMOHα) through a β4 and an α1 helix (Fig. 2, A and B). The side chain of Gln[45] and the peptide backbone of residues 48 and 49 in MMOD β4 formed hydrogen bonds with Thr[241], Glu[240] (helix F), and Asn[214] (helix E) of MMOHα (Fig. 2B). Side chains and the backbone of MMOD Leu[50] and Ser[51] (MMOD loop) participated in hydrophobic and hydrogen bond interactions with Trp[317] and Asp[312] (helix H) of MMOHα (Fig. 2C). In the long α helix of MMOD, residues including Ser[54], His[61], Ser[64], His[65], Arg[68],
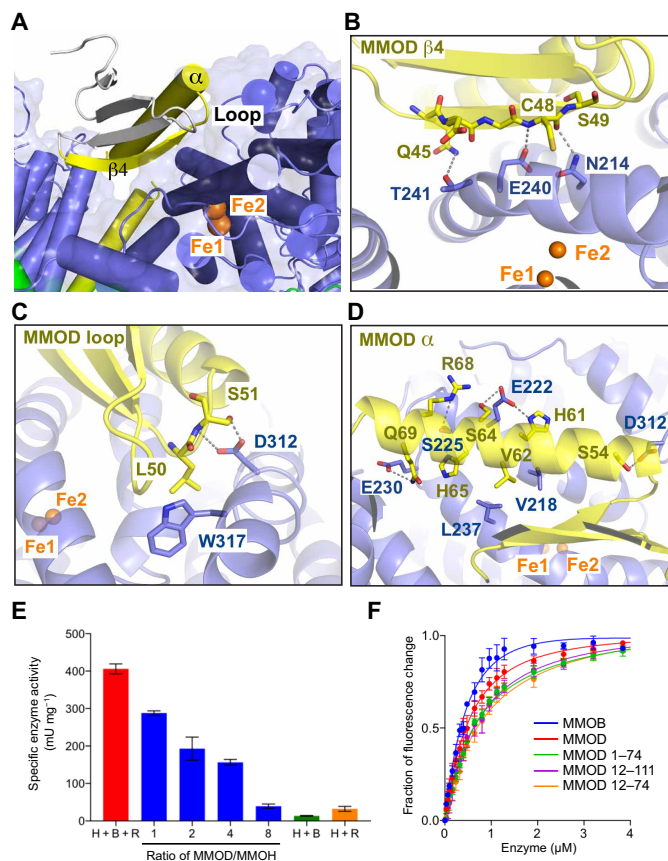

Fig. 2. Key residues participate in both the MMOH-MMOD binding and the inhibitory activity of MMOD. (A) MMOD β4, loop, and helix α (yellow) directly participate in recognizing the canyon region of MMOH. MMOD residues that do not interact with MMOH are colored gray. The two iron atoms are labeled and colored orange. (B to D) Detailed molecular interactions in the MMOH-MMOD complex. (E) Enzymatic activities (n = 3) of MMOH in the presence of MMOB, MMOR, and/or MMOD, as determined on the basis of the conversion from propylene to propylene oxide in the presence of NADH. Condition H + B + R (red) indicates the absence of MMOD; blue indicates the addition of MMOD. Conditions H + B (green) and H + R (orange) represent the absence of MMOR and MMOB, respectively (n = 3, average ± SEM). (F) Binding of MMOB, MMOD, and truncated MMODs to MMOH as detected by fluorescence spectroscopy (n = 3). All error bars represent SEMs. Quenching of intrinsic fluorescence of MMOH was monitored by titration of MMOB (blue), MMOD (red), 1 to 74 MMOD (green), 12 to 111 MMOD (purple), and 12 to 74 MMOD (orange). The dissociation constant (K_{d1} and K_{d2}) values were determined through nonlinear curve fitting for the two binding sites of MMOH (0.32 μM).

Gln[69] (hydrogen bond), and Val[62] (hydrophobic) interacted with Asp[312] (helix H), Val[218], Glu[222], Ser[225] (helix E), Glu[230], and Leu[237] (helix F) of MMOHα (Fig. 2D).

MMOD shares binding sites with MMOB

The crystal structure of the MMOH-MMOB complex demonstrated that MMOB also associated with the canyon region of MMOH generated by two MMOHα (fig. S2A) (14). A structural comparison between the MMOH-MMOB and MMOH-MMOD complexes strongly indicated that MMOD and MMOB competed for binding at the canyon region of MMOH, thereby partly inhibiting the catalytic activity of MMOH (fig. S2B). The catalytic activity of MMOH was reduced in the presence of increasing amounts of MMOD, as reported earlier

in *Methylococcus capsulatus* (Bath) sMMO counterparts (Fig. 2E) (*11*, *16*). The affinity measurements of MMOB and MMOD toward MMOH using fluorescence quenching of MMOH demonstrated comparable dissociation constants (Fig. 2F and table S2). The truncated MMODs (residues 1 to 74, 12 to 111, and 12 to 74) displayed slightly, but not substantially, reduced binding affinities, suggesting that the conserved core region of MMOD observed in the crystal structure is essential for MMOH recognition (table S2).

MMOD binding disorganizes MMOHβ-NT and disrupts di-iron coordination

To illustrate the influence of MMOD binding on the overall architecture of MMOH as well as the geometry of the di-iron center, we compared the structures of MMOH and the MMOH-MMOD complex. This comparison revealed a major conformational change in the N terminus of the MMOHβ (MMOHβ-NT) (Fig. 3A). Specifically, MMOHβ-NT would become disordered upon MMOD binding (Fig. 3A). A clash between the N-terminal helix of MMOHβ and the C-terminal long helix of MMOD resulted in MMOHβ-NT being pushed away, thereby dissociating it from MMOHα (Fig. 3, A and B). Since MMOHβ-NT functions as a "latch" to hold and maintain the structural integrity of MMOHα (Fig. 3A), the disorder of MMOHβ-NT (residues 1 to 56 of the β subunit) triggered structural relaxation in MMOHα and subsequent conformational changes, particularly at helices A, B, and C (Fig. 3B and fig. S3A). The di-iron center at MMOHα was coordinated by four glutamates and two histidines provided by
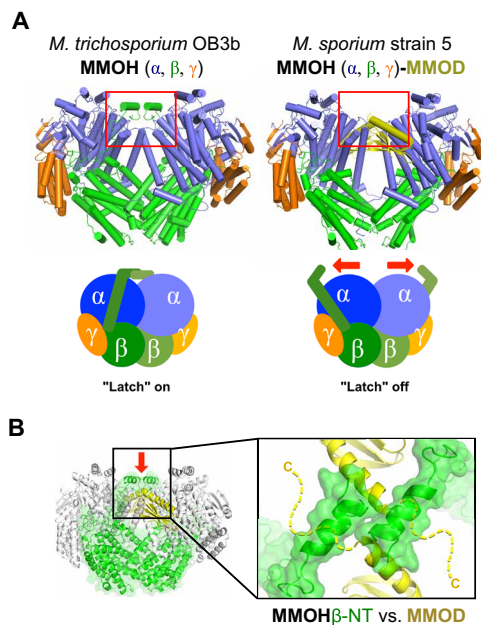
the four-helix bundle composed of helices B, C, E, and F (Fig. 4A). The conformational changes in helices B and C, triggered by the dissociation of MMOHβ-NT from MMOHα, led to geometric changes in the di-iron center and rearrangement of the di-iron coordination (Fig. 4, A and B). Particularly, His[147] (helix C) displayed a substantial conformational change that led to its dissociation from Fe1 coordination and allowed one water molecule to bridge in between Fe1 and His[147] (Fig. 4B). Since Fe1 maintained the full occupancy at the di-iron center, Fe1 was seemingly still stably incorporated at the di-iron center through this water bridge. The glutamate residues that coordinated the two iron atoms also rearranged their coordination upon MMOD association. For example, upon MMOD binding, both Glu[114] and Glu[144] recognized Fe1 in a chelating manner through the carboxylate shift, owing to the movement of helix B and C, respectively (Fig. 4, A and B, and fig. S3, A and B). In addition, Glu[243] interacted with Fe2 in a bidentate manner. To the best of our knowledge, the dissociation of His[147] and bidentate coordination of Glu[114] unraveling in the MMOH-MMOD complex have not been observed in previous MMOH-related structures (Fig. 4B, fig. S4, and table S3). Notably, the dissociation of His[147] from the di-iron active site (Fe1–His[147] Nδ1 distance within two protomers: 5.27 Å/4.98 Å) could further inhibit the catalytic activity of MMOH.
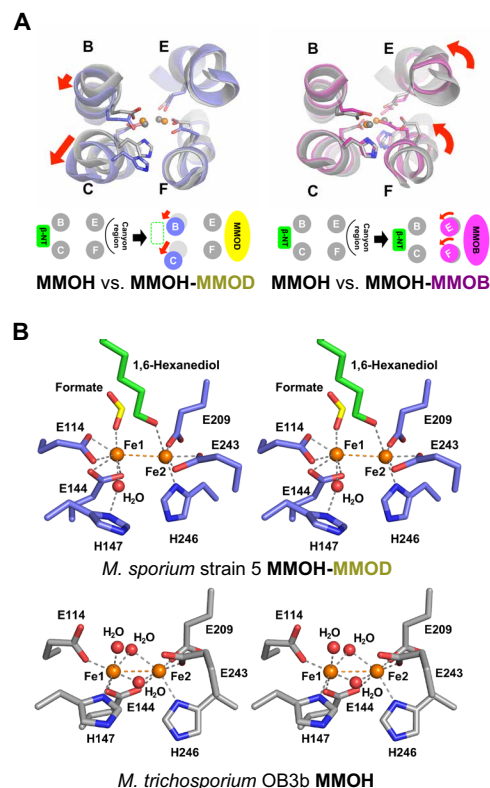

Fig. 3. Structural comparison of MMOH (PDB ID: 1MHY) (*20*) and the MMOH-MMOD complex. (**A**) Front views of MMOH and MMOH-MMOD. Red box indicates the region with the major structural differences. The schematic model shows that MMOHβ-NT functions as a latch to tightly lock the MMOHα helix bundles. MMOD binding unlocks the latch and relaxes the overall helix architecture of MMOHα. (**B**) *M. sporium* strain 5 MMOD structures are overlaid onto *M. trichosporium* OB3b MMOH. The N terminus of MMOHβ is displayed in green. The MMOD C-terminal long helix is shown in yellow. Dashed yellow lines indicate the extended, disordered C-terminal region of MMOD. The red arrow indicates the viewing angle of the inset. The inset shows the clash between MMOHβ-NT and the C-terminal helix of MMOD.

Fig. 4. Structural comparison of the di-iron center of MMOH (PDB ID: 1MHY) (*20*), MMOH-MMOB (PDB ID: 4GAM) (*14*), and MMOH-MMOD. (**A**) Conformational changes in the MMOH four-helix bundle (helices B, C, E, and F) upon MMOB and MMOD binding. Six residues that coordinate to the two iron atoms are on helices B, C, E, and F. Red arrows indicate the translation and rotation of the indicated helices upon MMOD and MMOB binding. (**B**) Stereo views of the di-iron center geometry in MMOH-MMOD and MMOH. The two Fe atoms (orange) are surrounded and coordinated by four glutamate and two histidine residues. Water molecules (H₂O) are displayed as red spheres.

MMOD and MMOB binding differently rearrange the four-helix bundle

The extent of structural reorganization in the di-iron center caused by MMOD binding was comparable to that caused by MMOB binding. It was found that the binding of MMOB induced conformational changes at helices E and F, which subsequently pushed Glu[243] (helix F) into the di-iron center (Fig. 4A and fig. S3, A and B). Consequently, this change squeezed the two Fe atoms of the center between Glu[243] (helix F) and Glu[144] (helix C), leading to a change in the reduction potential at the di-iron center (fig. S3C) (15). While MMOB binding induced the rotation of helices E and F, the MMOD binding disorganized MMOHβ-NT, thereby allowing the translational movement of helices B and C (fig. S3B). As a consequence, MMOD binding inhibited the catalytic activity of MMOH, while MMOB binding optimized the di-iron geometry for its catalysis, although both the inhibitor and activator associated at the same binding pocket located at MMOHα.

1,6-Hexanediol at the MMOHα cavities may mimic the MMOH product

Upon building the model structure of the MMOH-MMOD complex, we detected unidentified electron density near the di-iron center. When 1,6-hexanediol (one of the compounds used in the crystallization) was placed over this unknown electron density, a good fit was obtained after refinement (Fig. 5A). sMMO is known to oxidize a variety of hydrocarbons, including alkanes ranging from methane to octane. The presence of 1,6-hexanediol near the di-iron center can

be explained by the opening of the cavity, mediated by the side-chain rearrangement of Leu[110] and Phe[188], both of which function together as a gate for substrate and product passage to the active site (Fig. 5B) (14, 19, 25). A similar type of cavity opening was also observed in the MMOH-MMOB complex (fig. S5, A and B) (14). While MMOB is known to connect cavities for substrate access, the MMOD-mediated cavity opening appeared to be a consequence of MMOHβ-NT dissociation and subsequent structural relaxation of MMOHα (fig. S6). Examination of other previously reported product-soaked crystal structures of MMOH showed that the products or product analogs are mostly trapped in the cavities as a result of the closure mediated by Leu[110] and Phe[188] (Fig. 5C). In contrast, 1,6-hexanediol was able to reach the di-iron center via the substrate access cavity in the MMOH-MMOD complex because the binding of MMOD connected these cavities (Fig. 5B). The present MMOH-MMOD structure also supported the hypothesis that both substrate ingress and product egress may take place through the substrate access cavity and not through the pore located near the active site, at least for hydrocarbon chain substrates such as hexane (25).

DISCUSSION

The crystal structure of the MMOH-MMOD complex presented here strongly supports the inhibitory role of MMOD. MMOD binding leads to steric hindrance with the N-terminal region of MMOHβ, which then triggers the detachment of MMOHβ-NT from MMOHα
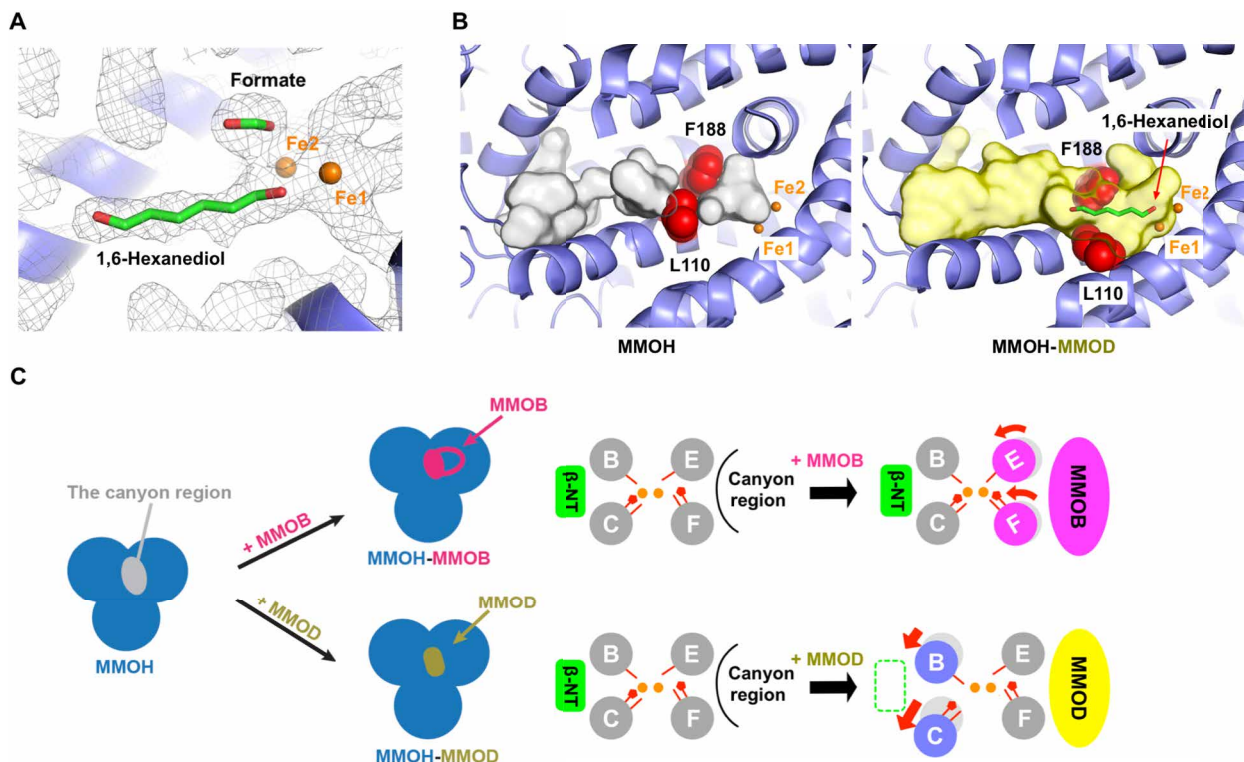

Fig. 5. Product analog 1,6-hexanediol at the substrate access cavity near the di-iron center and the cavity opening in the MMOH-MMOD complex. (**A**) Composite omit map [1.5σ contour, calculated using the PHENIX software package (38)] of MMOH-MMOD near the di-iron center. The electron density map is shown as a mesh (gray), and 1,6-hexanediol and formate are colored green. (**B**) Substrate access cavity in the *M. trichosporium* OB3b MMOH (gray, PDB ID: 1MHY) (20) and the *M. sporium* strain 5 MMOH-MMOD complex (yellow). The two gate-forming residues (Leu[110] and Phe[188]) are shown as red spheres, and 1,6-hexanediol is shown in green. The cavities calculated using PyMOL are shown as surface models. (**C**) Schematic model showing the association of MMOH with its auxiliary proteins MMOB and MMOD, which compete for the canyon region of MMOH.

("latch off"). Without the physical support of MMOHβ-NT, the overall structural integrity of MMOHα is perturbed, particularly at helices B and C within the four-helix bundle. The translational movement of helices B and C, which provides residues for the di-iron coordination, leads to geometric changes in the di-iron center, including His[147] dissociation from Fe1 coordination (Fig. 4B). We predict that the impaired di-iron center no longer activates O_2 to perform its oxidation toward hydrocarbon substrates.

MMOD has also been proposed as an iron assembly factor for MMOH based on the observation that the expression level of MMOD is relatively low and it binds tightly with MMOH near the di-iron center (11). However, iron reconstitution experiments using apoMMOH (iron removed) in the presence of MMOD or MMOB demonstrated that both MMOD and MMOB block iron loading toward apoMMOH instead of promoting it (11, 16). We also observed that both iron atoms show full occupancy at the di-iron center during structure refinement, indicating that there is no loss of iron upon MMOD association. One potential function is that MMOD acts as a protein chaperone to assist the protein folding of MMOH by protecting MMOH until MMOHβ-NT "latches on" as the final step of the protein folding process. However, the potential function of MMOD as a protein chaperone needs to be further explored in the near future.

Although the *orfY* gene (MMOD) is present within the sMMO operon (Fig. 1A), the fact that the protein expression level of MMOD is low and sMMO can perform its full catalytic reaction without it has raised questions about the active role of MMOD as a part of the sMMO catalytic system (26). Quantitative Western blot analysis of MMOD using cell lysates of *M. capsulatus* (Bath) grown under low copper conditions successfully detected the expression of endogenous MMOD, but its expression level was lower than that of MMOH (about 2 to 3% of the total MMOH expression) (11). Northern blot of the total mRNA transcriptions from *M. capsulatus* (Bath) grown in copper-deficient conditions detected three different types of mRNAs; mRNA1 contains *mmoX* (MMOHα); mRNA2 encodes *mmoX*, *mmoY*, *mmoB*, and *mmoZ* (MMOH and MMOB); and mRNA3 harbors all six genes (MMOH, MMOB, MMOD, and MMOR) (27).

The Lippard group showed that MMOD functions as an inhibitor against MMOH by competing with MMOB, as well as by potentially influencing the di-iron geometry (11). MMOD also has been proposed as a copper-switch (17, 18). The protein expression of pMMO and sMMO in methanotrophs can be switched depending on copper availability within the cells (27). Under low cellular copper concentration, sMMO genes are activated, while pMMO genes are suppressed and vice versa under high cellular copper concentration. Methanobactins, low–molecular weight (<1200 Da) copper-binding peptides that are overexpressed under low copper circumstances, have also been known to play a role in the copper-dependent pMMO/sMMO switch mechanism (17). MMOD has been proposed as a copper-switch protein based on the facts that (i) MMOD has no known function except its proposed inhibitory role and that (ii) the primary sequence of MMOD is predicted to associate with DNA (17). However, neither the DNA binding ability of MMOD nor its association with copper—the two key features that are required for acting as a direct copper-switch—have been directly measured.

The Rosenzweig group recently examined the DNA and copper interactions of MMOD but failed to detect copper binding (inductively coupled plasma mass spectrometry using recombinant MMOD purified either in the presence or absence of 5 mM $CuSO_4$) and DNA association (heparin column binding). When structurally homologous proteins of MMOD were searched using PDBeFold (28), two DNA binding proteins, λ integrase and the GCC-box binding domain, showed up as top candidates (fig. S7A). However, subsequent structural overlays with these DNA binding proteins demonstrated that MMOD cannot fit into the major groove region of DNA because of steric hindrance (fig. S7B). Expectedly, the electrophoretic mobility shift assays (EMSAs) failed to detect DNA association with MMOD (fig. S7C). Monitoring the copper incorporation of MMOD using the ultraviolet (UV)–visible spectrophotometer also indicated that MMOD does not bind with copper (fig. S7D). Therefore, it seems that MMOD does not function as a primary copper-switch by associating with copper and/or promoters directly. We cannot rule out, however, the possibility that MMOD may indirectly function as a copper-switch via as yet unknown mechanisms.

The crystal structures of the MMOH-MMOB and MMOH-MMOD complexes indicate that MMOB and MMOD associate with the canyon region of MMOH. The results of hydrogen-deuterium exchange mass spectrometry analysis and computational docking studies in the MMOH-MMOR complex indicate that MMOR also associates with the canyon region of MMOH (29). This suggests that all three auxiliary proteins of sMMO bind to the canyon region of MMOH for their regulatory roles (Fig. 5C).

The MMOH-MMOD structure determined in this work indicates that MMOD functions as an inhibitor for MMOH by competing with MMOB for MMOH association as well as by disrupting the active geometric form of the di-iron center (Fig. 5C). Together, the crystal structure of the MMOH-MMOD complex and the MMOH-MMOB structure determined previously demonstrate the mechanism by which auxiliary proteins modulate the catalytic activity of MMO hydroxylase, which involves inducing different conformational changes in MMOH as well as at the di-iron center.

MATERIALS AND METHODS
M. sporium strain 5 fermentation and purification of MMOH
M. sporium strain 5 [American Type Culture Collection (ATCC) 35069] was cultured in nitrate mineral salt media (ATCC 1306) at 30°C until optical density at 655 nm reached 8 to 10 with a methane:air (v/v) ratio of 10 to 15%. The cells were harvested by centrifugation (11,300g) for 20 min at 4°C. The cell pellets were suspended in a lysis buffer containing Mops (25 mM), NaCl (25 mM), sodium thioglycolate (8 mM), L-cysteine (2 mM), $(NH_4)_2Fe(SO_4)_2\cdot6H_2O$ (200 μM), $MgCl_2$ (5 mM), deoxyribonuclease (DNase) (0.25 μl/ml), and phenylmethylsulfonyl fluoride (PMSF, 0.04 mg/ml) at pH 6.5. The cell suspension was sonicated at 4°C (CV334 model, Sonics), and the lysate was centrifuged at 30,000g for 45 min at 4°C. The supernatant was carefully decanted and filtered through a 0.22-μm membrane (Merck Millipore). The filtrate was loaded onto DEAE Sepharose Fast Flow, Superdex 200, and Q Sepharose Fast Flow columns attached to the ÄKTA Pure 25 L fast protein liquid chromatography system (GE Healthcare) to purify MMOH with >95% purity (30). The purified MMOH was applied to a ferrozine assay to monitor the iron-ferrozine complex (562 nm), and the results revealed 3.9 to 4.2 Fe/MMOH with coefficient of determination (R^2) values >0.999 (14).

Expression and purification of MMOB and MMOR
Both recombinant *mmoB* (MMOB) and *mmoC* (MMOR) in a pET30a(+) plasmid were transformed into *Escherichia coli* BL21(DE3)

cells (Novagen) and cultured in LB media containing kanamycin (50 μg/ml) at 37°C. The cultures were induced for 5 hours with 1.0 mM isopropyl β-D-1-thiogalactopyranoside before harvesting by centrifugation at 4°C. The MMOB cell pellets were resuspended in solution containing phosphate (pH 6.0, 25 mM), NaCl (75 mM), MgCl$_2$ (5 mM), Na$_2$-EDTA (1 mM), dithiothreitol (DTT, 1 mM), DNase I (0.25 μl/ml), and PMSF (0.04 mg/ml). The suspended cells were lysed by sonication at 4°C. The filtered supernatant was applied to Q Sepharose Fast Flow and Superdex 75 columns (GE Healthcare) to obtain MMOB with >95% purity (23, 31). The MMOR cell pellets were resuspended in solution containing Mops (pH 6.5, 25 mM), sodium thioglycolate (8 mM), L-cysteine (2 mM), NaCl (25 mM), (NH$_4$)$_2$Fe(SO$_4$)$_2$·6H$_2$O (200 μM), MgCl$_2$ (5 mM), DNase I (1 U/ml), and PMSF (0.2 mM) and subsequently were sonicated for cell lysis. The lysed cells were centrifuged at 26,000g at 4°C for 40 min, filtered (0.22-μm membrane filter), and loaded onto DEAE Sepharose Fast Flow and Q Sepharose columns to purify MMOR (32). The ferrozine assay confirmed 2.1 to 2.2 Fe/MMOR with R^2 values >0.999 (30).

Activity measurement of MMOH

MMOH (1.0 μM), MMOB, (2.0 μM) and MMOR (0.5 μM) were added to a 25 mM solution of Mops (pH 7.5) containing DTT (1 mM) and NaCl (10 mM), and propylene gas was bubbled through the mixture (Hankook Special Gas) for 20 min. Subsequently, the mixture was incubated at 25°C. Steady-state kinetics were measured using a Cary 60 UV-visible spectrometer by the addition of NADH at 340 nm (extinction coefficient = 6220 cm^{-1} M^{-1}). The inhibitory activities of MMOD were measured in the absence or presence of progressively increasing amounts of MMOD. Products were confirmed by gas chromatography (YL 6500 GC system) using an Agilent HP-PLOT Q stationary column (30 m by 0.535 mm by 40.00 μm). Independent experiments were repeated in triplicate to calculate the mean and the SEM.

MMOD expression and purification

The N-terminal (His)$_{X6}$ and maltose-binding protein (hisMBP)–tagged wild-type *mmoD* (MMOD) was prepared in *E. coli* Rosetta (DE3) with auto-inducible media (33). Cell pastes were resuspended in solution containing tris-HCl (pH 7.5, 30 mM), NaCl (500 mM), and β-mercaptoethanol (5 mM) with protease inhibitor cocktails. After sonication on ice for 3 min, soluble lysate was recovered by centrifugation at 20,000g for 30 min and was subsequently applied to a cobalt affinity resin (Takeda). The hisMBP-MMOD proteins were eluted with elution buffer [tris-HCl, 30 mM (pH 7.5); NaCl, 500 mM; imidazole, 300 mM; and β-mercaptoethanol, 5 mM]. To remove the hisMBP tag, we mixed the elution fraction and tobacco etch virus protease (1:100 ratio) together in the amylose resin. After overnight incubation at 4°C, the flow-through fraction, which contains MMOD, was collected from the amylose resin and loaded onto an HP Q column (GE Healthcare); equilibrated with Hepes (pH 7.5, 30 mM), NaCl (100 mM), and DTT (1 mM); and eluted in a 0 to 1000 mM NaCl gradient. On the basis of the results of SDS–polyacrylamide gel electrophoresis, fractions containing MMOD were pooled. The pooled fractions were then concentrated using Amicon (EMD Millipore) and applied to a Superdex 200 (10/300) size exclusion chromatography (GE Healthcare) column equilibrated in Hepes (pH 7.5, 30 mM), NaCl (100 mM), and tris(2-carboxyethyl) phosphine (TCEP, 1 mM).

Crystallization, data collection, and structure determination

Purified MMOH and MMOD [in solution containing Hepes, 30 mM (pH 7.5); NaCl, 100 mM; and TCEP, 1 mM] were mixed in a 1:2 molar ratio, and the final concentration was adjusted to 10 mg/ml. Plate-shaped crystals were grown within a week at room temperature using the hanging drop vapor diffusion method with a mixture of 10% (w/v) PEG 8000 (polyethylene glycol, molecular weight 8000), 20% (v/v) ethylene glycol, 0.02 M 1,6-hexanediol, 0.02 M 1-butanol, 0.02 M 1,2-propanediol, 0.02 M 2-propanol, 0.02 M 1,4-butanediol, 0.02 M 1,3-propanediol, 0.89 M 1,3-butanediol, and 0.1 M MES/imidazole buffer (pH 6.5). After transferring to a cryoprotectant solution containing the precipitant and 35% (w/v) PEG 8000, crystals were flash-frozen in liquid nitrogen. The space group of the crystal was C$_2$ with *a* = 179.8 Å, *b* = 125.8 Å, *c* = 126.4 Å, α = γ = 90°, and β = 102.9°. The dataset was collected at Advanced Photon Source on beamline Life Sciences Collaborative Access Team (LS-CAT) 21 ID-G. The 2.6-Å data were processed by HKL2000 (www.hkl-xray.com), and initial phases were calculated by molecular replacement (Phaser) (34) using *M. trichosporium* OB3b MMOH as the search model (PDB ID: 1MHY) (20). After molecular replacement, the electron density for MMOD was clearly visible. The MMOD model was subsequently manually built using COOT (35), and the refinement was performed using phenix.refine (36). Iron atoms and ligand restraints were generated using the program PHENIX (phenix.metal_coordination and phenix.ready_set) and applied during the refinement. No noncrystallographic symmetry restraints were applied during the refinement. The asymmetric unit contains two copies each of the MMOHα, MMOHβ, and MMOHγ subunits and MMOD full-length, and the R_{work} and R_{free} values of the final refined model were 17.8 and 22.6, respectively. Residues 1 to 11 (1 to 10) and 161 to 172 (159 to 171) of the MMOHα, residues 1 to 56 (1 to 56) of the MMOHβ, residues 1 to 4 (1 to 2) of the MMOHγ, and residues 1 to 11 (1 to 6) and 76 to 111 (75 to 111) of MMOD were disordered and invisible in the final model (parentheses indicate residues in the other MMOH protomer). Ramachandran analyses were performed by MolProbity (37), and the results were as follows: 95.4 (favored), 4.5 (allowed), and 0.1% (outlier).

Binding affinity measurements

The fluorescence spectra were collected at 25°C using the PTI QuantaMaster 400 (Horiba, Canada) with monochromators for both excitation and emission. Fluorescence spectra of MMOH [0.32 μM MMOH in 300 μl of 25 mM Mops (pH 7.0) and 1 mM DTT] were determined using an excitation wavelength of 282 nm. Fluorescence was quantified by the integration of fluorescence emission bands with a maximum at 363 nm. The MMOH fluorescence was quenched by titration with MMOB, MMOD, and truncated MMODs (residues 1 to 74, 12 to 111, and 12 to 74). These proteins were titrated against MMOH in the concentration range from 0 to 15 μM. Dissociation constants were determined by fitting the intensity of emission at 363 nm (Origin 2018b and Wolfram Mathematica). Independent experiments were repeated in triplicate to allow the calculation of the average ± SEM.

Electrophoretic mobility shift assay

EMSA was performed in a 30-μl reaction vessel containing 10 mM tris-HCl (pH 8.0), 1 mM EDTA, 50 mM NaCl, 2.5 mM MgCl$_2$, 5% glycerol, and 0.1 mM DTT. The final concentration of 0.2 μM DNA and 0.4 μM MMOD were mixed in the presence and absence of 0.1 mM CuCl$_2$.

The mixtures were then incubated at room temperature for 30 min and electrophoresed using a 10% nondenaturing polyacrylamide gel (mmoX1 DNA: 5′-TCAGTGGCACGAGGCTTGCCATAACAATA-AGCGTCGT-3′; mmoX2 DNA: 5′-ATTACGGCACACACCTTGCT-GTGAAAGAACCGACGTC-3′; and random DNA: 5′-CATGTTCT-GTCGCACTTTAAGCGTCAAGATGAGGCGG-3′).

Copper binding assay of MMOD

Metal-binding titrations of MMOD and copper were performed in quartz cuvettes using a UV-visible spectrophotometer (Cary 60, Agilent, USA). The optical spectra of MMOD (10 μM) were measured by titration of 1.0 equimolar concentrations of $CuCl_2 \cdot (H_2O)_2$ (Sigma-Aldrich, 99.999%) in 750-μl buffer (25 mM sodium phosphate at pH 7.0).

SUPPLEMENTARY MATERIALS

Supplementary material for this article is available at http://advances.sciencemag.org/cgi/content/full/5/10/eaax0059/DC1

Table S1. Data collection and refinement statistics.
Table S2. Dissociation constants for binding of MMOH and MMOB, MMOD, and truncated MMOD proteins.
Table S3. Active-site Fe-Fe distances in MMOH structures.
Fig. S1. Primary sequence conservation of *M. trichosporium* OB3b and *M. sporium* strain 5 MMOHs and multiple sequence alignment of MMOD.
Fig. S2. Crystal structure of the *M. capulatus* MMOH-MMOB complex (PDB ID: 4GAM) and the structural comparison of MMOD (*M. sporium* strain 5) and MMOB (*M. capsulatus*) binding to MMOH.
Fig. S3. Conformational changes in MMOH upon MMOD and MMOB binding.
Fig. S4. Geometry of the di-iron active site in the MMOH-MMOD complex and its structural comparison with other known MMOH structures.
Fig. S5. Comparison of the substrate access routes in MMOH (PDB ID: 1MHY), MMOH-MMOB complex (PDB ID: 4GAM), and MMOH-MMOD complex.
Fig. S6. Comparison of the internal cavities within the MMOH protomer of MMOH-MMOD complex, MMOH, and MMOH-MMOB complex.
Fig. S7. MMOD does not associate with DNA as well as copper ions.
References (*39*, *40*)

REFERENCES AND NOTES

1. R. S. Hanson, T. E. Hanson, Methanotrophic bacteria. *Microbiol. Rev.* **60**, 439–471 (1996).
2. I. J. Higgins, D. J. Best, R. C. Hammond, New findings in methane-utilizing bacteria highlight their importance in the biosphere and their commercial potential. *Nature* **286**, 561–564 (1980).
3. V. C.-C. Wang, S. Maji, P. P.-Y. Chen, H. K. Lee, S. S.-F. Yu, S. I. Chan, Alkane oxidation: Methane monooxygenases, related enzymes, and their biomimetics. *Chem. Rev.* **117**, 8574–8621 (2017).
4. C. E. Tinberg, S. J. Lippard, Dioxygen activation in soluble methane monooxygenase. *Acc. Chem. Res.* **44**, 280–288 (2011).
5. S. Sirajuddin, A. C. Rosenzweig, Enzymatic oxidation of methane. *Biochemistry* **54**, 2283–2294 (2015).
6. A. J. Jasniewski, L. Que Jr., Dioxygen activation by nonheme diiron enzymes: Diverse dioxygen adducts, high-valent intermediates, and related model complexes. *Chem. Rev.* **118**, 2554–2592 (2018).
7. R. Banerjee, Y. Proshlyakov, J. D. Lipscomb, D. A. Proshlyakov, Structure of the key species in the enzymatic oxidation of methane to methanol. *Nature* **518**, 431–434 (2015).
8. M. Merkx, D. A. Kopp, M. H. Sazinsky, J. L. Blazyk, J. Muller, S. J. Lippard, Dioxygen activation and methane hydroxylation by soluble methane monooxygenase: A tale of two irons and three proteins. *Angew. Chem. Int. Edit.* **40**, 2782–2807 (2001).
9. D. E. Coufal, J. L. Blazyk, D. A. Whittington, W. W. Wu, A. C. Rosenzweig, S. J. Lippard, Sequencing and analysis of the *Methylococcus capsulatus* (Bath) soluble methane monooxygenase genes. *Eur. J. Biochem.* **267**, 2174–2185 (2000).
10. W. A. Froland, K. K. Andersson, S.-K. Lee, Y. Liu, J. D. Lipscomb, Methane monooxygenase component B and reductase alter the regioselectivity of the hydroxylase component catalyzed reactions: A novel role for protein-protein interactions in an oxygenase mechanism. *J. Biol. Chem.* **267**, 17588–17597 (1992).
11. M. Merkx, S. J. Lippard, Why OrfY? Characterization of MMOD, a long overlooked component of the soluble methane monooxygenase from *Methylococcus capsulatus* (Bath). *J. Biol. Chem.* **277**, 5858–5865 (2002).
12. B. J. Wallar, J. D. Lipscomb, Dioxygen activation by enzymes containing binuclear non-heme iron clusters. *Chem. Rev.* **96**, 2625–2658 (1996).
13. D. A. Kopp, G. T. Gassner, J. L. Blazyk, S. J. Lippard, Electron-transfer reactions of the reductase component of soluble methane monooxygenase from *Methylococcus capsulatus* (Bath). *Biochemistry* **40**, 14932–14941 (2001).
14. S. J. Lee, M. S. McCormick, S. J. Lippard, U.-S. Cho, Control of substrate access to the active site in methane monooxygenase. *Nature* **494**, 380–384 (2013).
15. K. E. Paulsen, Y. Liu, B. G. Fox, J. D. Lipscomb, E. Munck, M. T. Stankovich, Oxidation-reduction potentials of the methane monooxygenase hydroxylase component from *Methylosinus trichosporium* OB3b. *Biochemistry* **33**, 713–722 (1994).
16. M. H. Sazinsky, M. Merkx, E. Cadieux, S. Tang, S. J. Lippard, Preparation and x-ray structures of metal-free, dicobalt and dimanganese forms of soluble methane monooxygenase hydroxylase from *Methylococcus capsulatus* (Bath). *Biochemistry* **43**, 16263–16276 (2004).
17. J. D. Semrau, S. Jagadevan, A. A. DiSpirito, A. Khalifa, J. Scanlan, B. H. Bergman, B. C. Freemeier, B. S. Baral, N. L. Bandow, A. Vorobev, D. H. Haft, S. Vuilleumier, J. C. Murrell, Methanobactin and MmoD work in concert to act as the 'copper-switch' in methanotrophs. *Environ. Microbiol.* **15**, 3077–3086 (2013).
18. A. A. DiSpirito, J. D. Semrau, J. C. Murrell, W. H. Gallagher, C. Dennison, S. Vuilleumier, Methanobactin and the link between copper and bacterial methane oxidation. *Microbiol. Mol. Biol. Rev.* **80**, 387–409 (2016).
19. A. C. Rosenzweig, C. A. Frederick, S. J. Lippard, P. Nordlund, Crystal structure of a bacterial nonheme iron hydroxylase that catalyses the biological oxidation of methane. *Nature* **366**, 537–543 (1993).
20. N. Elango, R. Radhakrishnan, W. A. Froland, B. J. Wallar, C. A. Earhart, J. D. Lipscomb, D. H. Ohlendorf, Crystal structure of the hydroxylase component of methane monooxygenase from *Methylosinus trichosporium* OB3b. *Protein Sci.* **6**, 556–568 (1997).
21. L. L. Chatwood, J. Müller, J. D. Gross, G. Wagner, S. J. Lippard, NMR structure of the flavin domain from soluble methane monooxygenase reductase from *Methylococcus capsulatus* (Bath). *Biochemistry* **43**, 11983–11991 (2004).
22. J. Müller, A. A. Lugovskoy, G. Wagner, S. J. Lippard, NMR structure of the [2Fe-2S] ferredoxin domain from soluble methane monooxygenase reductase and interaction with its hydroxylase. *Biochemistry* **41**, 42–51 (2002).
23. K. J. Walters, G. T. Gassner, S. J. Lippard, G. Wagner, Structure of the soluble methane monooxygenase regulatory protein B. *Proc. Natl. Acad. Sci. U.S.A.* **96**, 7877–7882 (1999).
24. R. G. Castillo, R. Banerjee, C. J. Allpress, G. T. Rohde, E. Bill, L. Que Jr., J. D. Lipscomb, S. DeBeer, High-energy-resolution fluorescence-detected x-ray absorption of the q intermediate of soluble methane monooxygenase. *J. Am. Chem. Soc.* **139**, 18024–18033 (2017).
25. M. H. Sazinsky, S. J. Lippard, Product bound structures of the soluble methane monooxygenase hydroxylase from *Methylococcus capsulatus* (bath): Protein motion in the α-subunit. *J. Am. Chem. Soc.* **127**, 5814–5825 (2005).
26. D. L. N. Cardy, V. Laidler, G. P. C. Salmond, J. C. Murrell, The methane monooxygenase gene cluster of *Methylosinus trichosporium*: Cloning and sequencing of the *mmoC* gene. *Arch. Microbiol.* **156**, 477–483 (1991).
27. A. K. Nielsen, K. Gerdes, J. C. Murrell, Copper-dependent reciprocal transcriptional regulation of methane monooxygenase genes in *Methylococcus capsulatus* and *Methylosinus trichosporium*. *Mol. Microbiol.* **25**, 399–409 (1997).
28. E. Krissinel, K. Henrick, Secondary-structure matching (SSM), a new tool for fast protein structure alignment in three dimensions. *Acta Crystallogr. D Biol. Crystallogr.* **60**, 2256–2268 (2004).
29. W. Wang, R. E. Iacob, R. P. Luoh, J. R. Engen, S. J. Lippard, Electron transfer control in soluble methane monooxygenase. *J. Am. Chem. Soc.* **136**, 9754–9762 (2014).
30. L. G. Beauvais, S. J. Lippard, Reactions of the peroxo intermediate of soluble methane monooxygenase hydroxylase with ethers. *J. Am. Chem. Soc.* **127**, 7370–7378 (2005).
31. H. Brandstetter, D. A. Whittington, S. J. Lippard, C. A. Frederick, Mutational and structural analyses of the regulatory protein B of soluble methane monooxygenase from *Methylococcus capsulatus* (Bath). *Chem. Biol.* **6**, 441–449 (1999).
32. J. L. Blazyk, S. J. Lippard, Domain engineering of the reductase component of soluble methane monooxygenase from *Methylococcus capsulatus* (Bath). *J. Biol. Chem.* **279**, 5630–5640 (2004).
33. F. W. Studier, Protein production by auto-induction in high density shaking cultures. *Protein Expr. Purif.* **41**, 207–234 (2005).
34. A. J. McCoy, R. W. Grosse-Kunstleve, P. D. Adams, M. D. Winn, L. C. Storoni, R. J. Read, Phaser crystallographic software. *J. Appl. Cryst.* **40**, 658–674 (2007).
35. P. Emsley, B. Lohkamp, W. G. Scott, K. Cowtan, Features and development of Coot. *Acta Crystallogr. D Biol. Crystallogr.* **66**, 486–501 (2010).
36. P. V. Afonine, R. W. Grosse-Kunstleve, N. Echols, J. J. Headd, N. W. Moriarty, M. Mustyakimov, T. C. Terwilliger, A. Urzhumtsev, P. H. Zwart, P. D. Adams, Towards automated crystallographic structure refinement with phenix. refine. *Acta Crystallogr. D Biol. Crystallogr.* **68**, 352–367 (2012).

37. V. B. Chen, W. B. Arendall III, J. J. Headd, D. A. Keedy, R. M. Immormino, G. J. Kapral, L. W. Murray, J. S. Richardson, D. C. Richardson, MolProbity: All-atom structure validation for macromolecular crystallography. *Acta Crystallogr. D Biol. Crystallogr.* **66**, 12–21 (2010).

38. P. V. Afonine, N. W. Moriarty, M. Mustyakimov, O. V. Sobolev, T. C. Terwilliger, D. Turk, A. Urzhumtsev, P. D. Adams, FEM: Feature-enhanced map. *Acta Crystallogr. D Biol. Crystallogr.* **71**, 646–666 (2015).

39. M. Petřek, M. Otyepka, P. Banáš, P. Košinová, J. Koča, J. Damborský, CAVER: A new tool to explore routes from protein clefts, pockets and cavities. *BMC Bioinformatics* **7**, 316 (2006).

40. E. A. Fadeev, M. D. Sam, R. T. Clubb, NMR structure of the amino-terminal domain of the lambda integrase protein in complex with DNA: Immobilization of a flexible tail facilitates beta-sheet recognition of the major groove. *J. Mol. Biol.* **388**, 682–690 (2009).

Citation: H. Kim, S. An, Y. R. Park, H. Jang, H. Yoo, S. H. Park, S. J. Lee, U.-S. Cho, MMOD-induced structural changes of hydroxylase in soluble methane monooxygenase. *Sci. Adv.* **5**, eaax0059 (2019).